BIOLOGICAL SCIENCES: Biophysics and Computational Biology

Stepwise Isotope Editing of [FeFe]-Hydrogenases Exposes Cofactor Dynamics

Moritz Senger[1], Stefan Mebs[2], Jifu Duan[3], Florian Wittkamp[4], Ulf-Peter Apfel[4], Joachim Heberle[1], Michael Haumann[2], Sven T. Stripp[1]*

[1]Department of Physics, Experimental Molecular Biophysics, Freie Universität Berlin, 14195 Berlin, Germany

[2]Department of Physics, Biophysics of Metalloenzymes, Freie Universität Berlin, 14195 Berlin, Germany

[3]Department of Biochemistry of Plants, Photobiotechnology, Ruhr-Universität Bochum, 44801 Bochum, Germany

[4]Department of Chemistry and Biochemistry, Inorganic Chemistry I, Ruhr-Universität Bochum, 44801 Bochum, Germany

**Correspondence to:*

Dr. Sven Stripp, Freie Universität Berlin, Fachbereich Physik, Arnimallee 14, 14195 Berlin, Germany, Phone: +49 30 838 55069, E–mail: sven.stripp@fu-berlin.de

Keywords: [FeFe]-hydrogenase, isotope editing, infrared spectroscopy, density functional theory, cofactor dynamics

Running title: Structural dynamics of the H-cluster

Abbreviations: adt, amine dithiolate; ATR-FTIR, attenuated total reflection Fourier-transform infrared spectroscopy; CPI, DDH, HYDA1, [FeFe]-hydrogenase protein from *C. pasteurianum*, *D. desulfuricans*, or *C. reinhardtii*; DFT, density functional theory; H-cluster, six-iron cofactor of [FeFe]-hydrogenases

Abstract

The six-iron cofactor of [FeFe]-hydrogenases (H-cluster) is the most efficient H_2-forming catalyst in nature. It comprises a diiron active site with three carbon monoxide (CO) and two cyanide (CN^-) ligands in the active oxidized state (H_{ox}) and one additional CO ligand in the inhibited state (H_{ox}-CO). The diatomic ligands are sensitive reporter groups for structural changes at the cofactor. Their vibrational dynamics were monitored by real-time attenuated total reflection Fourier-transform infrared spectroscopy. Combination of ^{13}CO gas exposure, blue or red light irradiation, and controlled hydration of three different [FeFe]-hydrogenase proteins produced eight H_{ox} and sixteen H_{ox}-CO species with all possible isotopic exchange patterns. Extensive density functional theory calculations revealed the vibrational mode couplings of the carbonyl ligands and uniquely assigned each infrared spectrum to a specific labeling pattern. For H_{ox}-CO, agreement between experimental and calculated infrared frequencies improved by up to one order of magnitude for an apical CN^- at the distal iron ion of the cofactor as opposed to an apical CO in crystal structures. For H_{ox}, two equally probable isomers with partially rotated ligands were suggested. Interconversion between these structures implies dynamic ligand reorientation at the H-cluster. Our experimental protocol for site-selective ^{13}CO isotope editing combined with computational species assignment opens new perspectives for characterization of functional intermediates in the catalytic cycle.

Significance Statement

[FeFe]-hydrogenases are H_2-forming enzymes with potential in renewable energy applications. Their molecular mechanism of catalysis needs to be understood. A protocol for specific ^{13}CO isotope editing of all carbon monoxide ligands at the six-iron cofactor (H-cluster) was established. Analysis of vibrational modes via quantum chemical calculations implies structural dynamics at the H-cluster in the active-ready state. Site-selective introduction of isotopic reporter groups opens new perspectives to identify intermediates in the catalytic cycle.

Introduction

[FeFe]–hydrogenases catalyze the reduction of protons to form molecular hydrogen (H_2) and vice versa (1, 2). With a turnover rate of up to 10.000 H_2 molecules per second in a thermodynamically reversible reaction (3-5). [FeFe]-hydrogenases are inspiring synthetic hydrogen catalysts (6-8) and renewable fuel technology applications (9, 10). The mechanism of catalysis at their active-site cofactor (H-cluster) needs to be elucidated. Further information on functional intermediates is required (11-16) and expected to emerge from spectroscopic studies on H-cluster constructs carrying site-selective isotopic reporter groups (17-20).

Protein crystallography has identified the H-cluster as a six-iron complex (21-23), in which a canonical cubane cluster ($[4Fe4S]_H$) is linked to a unique diiron moiety ($[2Fe]_H$) (Fig. 1). The two iron ions of $[2Fe]_H$ are located in proximal (*p*) or distal (*d*) position relative to $[4Fe4S]_H$ and carry a bridging amine-dithiolate group (adt, $(SCH_2)_2NH$) (19). Both iron ions bind a terminal carbonyl (CO) and a cyanide (CN^-) ligand. In crystal structures, the "active-ready", oxidized state (H_{ox}) of the H-cluster shows a third carbonyl in Fe-Fe bridging position (μCO) and an apical vacancy at Fe_d (23). Upon exposure to CO gas, a fourth carbonyl binds at $[2Fe]_H$ (24-26) and was modeled in apical position at Fe_d in H_{ox}-CO (27). Formation of H_{ox}-

CO does not affect the formal redox state of the H-cluster, but leads to increased spin delocalization over the diiron site (28). CO binding inhibits H_2 turnover and protects the enzyme against O_2 and light-induced degradation (24, 29, 30).

The vibrational modes of the CO and CN^- ligands at the diiron site are well accessible by infrared (IR) spectroscopy because they are separated from protein backbone and liquid water bands. Infrared spectroscopy therefore has pioneered elucidation of the molecular structure of the H-cluster and identification of several redox states (24, 31). In particular the CO stretching frequencies are highly sensitive to structural isomerism, redox transitions, ligand binding, and isotope exchange (11, 12, 15, 18, 24, 31, 32). ^{13}CO editing of the H-cluster has been achieved using ^{13}C-precursors during H-cluster assembly or exposure of [FeFe]-hydrogenases to ^{13}CO gas (18, 24-26, 33). This has yielded either a completely labeled H-cluster, mixtures of labeled species, and mostly the inhibited state. Selective ^{13}CO editing of H_{ox} was hampered by tight binding of exogenous CO, which impaired quantitative regeneration of active enzyme (29, 34). H_{ox} is believed to be the starting state in the H_2 conversion cycle of [FeFe]-hydrogenases (1). Selective ^{13}CO editing of H_{ox} thus may provide access to key catalytic H-cluster intermediates (14). Introduction of ^{13}CO groups also facilitates analysis of structure-function relationships using quantum chemical calculations. However, relatively few computational studies to calculate vibrational modes of the diatomic ligands have been carried out (35-39).

We compared three different [FeFe]-hydrogenase proteins, HYDA1 from the green alga *Chlamydomonas reinhardtii* and the bacterial enzymes CPI from *Clostridium pasteurianum* and DDH from *Desulfovibrio desulfuricans*. HYDA1 represents the “minimal unit” of biological hydrogen turnover as it binds only the H-cluster while CPI and DDH hold accessory iron-sulfur clusters (3, 40). Purified HYDA1 and CPI were reconstituted *in vitro* with a synthetic diiron site analogue to yield the active H-cluster (35, 41, 42) whereas DDH

was isolated with a complete cofactor (43). We report the generation of H_{ox}-CO and H_{ox} isotopic species with all possible labeling patterns upon exposure of [FeFe]-hydrogenase protein films to ^{13}CO gas, visible light, and different levels of humidity as monitored by real-time attenuated total reflection Fourier-transform infrared spectroscopy (ATR-FTIR). Density functional theory (DFT) assigned the carbonyl vibrational modes. This has established a reaction scheme with 16 options to convert selectively labeled H_{ox}-CO into 8 H_{ox} isotopic species as entry points to the catalytic cycle.

Results

[FeFe]-hydrogenase protein films deposited on an ATR cell were exposed to ^{12}CO, ^{13}CO, or N_2 gas with controlled humidity either in darkness or under red or blue light irradiation, exploring the differential wavelength sensitivity of the iron-carbonyl bonds (44). Real-time detection of spectral changes of the stretching vibrations of the diatomic ligands (SI Appendix, Figs. S1-S4) yielded high-quality IR spectra of the thereby derived pure H_{ox} and H_{ox}-CO states (Fig. 2). Frequencies and intensities of IR bands were determined using least-squares fitting. Density functional theory calculations generated geometry-optimized models of the whole H-cluster for H_{ox}-CO and H_{ox} (SI Appendix, Fig. S5). Calculated IR spectra were used for assignment of experimental vibrational bands to individual CO ligands, specific isotopic labeling patterns, and molecular structures.

IR band assignment for unlabeled H_{ox} and H_{ox}-CO. Under an N_2 atmosphere HYDA1 showed the typical three CO bands of the H_{ox} state (Fig. 2A, **i**). Carbonyl bands shifted by ~40 cm^{-1} to lower frequencies due to ^{13}CO isotope editing (see below) whereas the CN^- bands shifted less than 1 cm^{-1} (SI Appendix, Fig. S6) and hence were not decisive for H-cluster species assignment. DFT consistently attributed the CO bands to the largely uncoupled

vibrations of the Fe-Fe bridging carbonyl (μCO, band α at 1802 cm^{-1}) and the terminal CO ligands at Fe_d (*d*CO, band β at 1940 cm^{-1}) and Fe_p (*p*CO, band γ at 1964 cm^{-1}) (SI Appendix, Fig. S9). As a measure for correlation of calculated and experimental CO frequencies the root-mean-square-deviation (rmsd, Eq. S1) was calculated (Tables 1 and SI Appendix, Table S1 and Fig. S11). A mean rmsd of ~10 cm^{-1} was obtained for the four possible H_{ox} rotamers with equatorial CO/CN^- ligands at Fe_p and Fe_d (Fig. 3A). This indicated good agreement between experimental and calculated CO frequencies. A similar small rmsd was obtained for a H_{ox} rotamer with *d*CN^- rotated towards a more apical position (Fig. 4), whereas a rotated apical *d*CO was disfavored. In the following, H-cluster rotamer structures are discussed relative to the "standard" model (24, 25, 45) with *trans* orientation of equatorial CO ligands and apical vacancy at Fe_d in H_{ox} (Fig. 1).

Exchange of N_2 by ^{12}CO gas in the headspace above the protein film resulted in the appearance of a forth CO band (δ) at higher IR frequencies due to an additional carbonyl ligand (d_2CO) in H_{ox}-CO (Fig. 2A, **xii**). We calculated the IR bands of the six possible CO/CN^- rotamers. Similar large rmsd values (~30 cm^{-1}) were observed for the four structures with apical d_2CO (Tables S2). An about six-fold improved rmsd (~5 cm^{-1}) was observed for the H_{ox}-CO structure with apical *d*CN^- and d_2CO in the equatorial plane (Fig. 3B). DFT assigned band α to the μCO stretch mode (1808 cm^{-1}) and band β to an anti-symmetric coupled mode with smaller contributions from equatorial d_1CO and larger contributions from apical d_2CO (1962 cm^{-1}). Band γ was assigned to a coupled mode with similar contributions from the symmetric vibrations of d_1CO and d_2CO and the anti-symmetric stretch mode of *p*CO (1968 cm^{-1}), and band δ to a coupled symmetric mode with contributions from all four carbonyls (2012 cm^{-1}) in the "standard" model (SI Appendix, Fig. S9). Except for the energetically separated band α due to the μCO ligand (SI Appendix, Fig. S7), pronounced

vibrational coupling of d_1CO, d_2CO, and pCO precludes *a priori* assignment of IR bands to specific CO ligands in H_{ox}-CO.

Stepwise ^{13}CO editing of the H-cluster. For HYDA1 protein films, exposure of unlabeled H_{ox}-CO (**xii**) to ^{13}CO gas caused a >20 cm^{-1} shift to lower frequencies of bands β and δ while band γ was less affected and α remained unchanged, suggesting a single ^{13}CO ligand at Fe_d (Fig. 2A, **ii**). Red light irradiation under ^{13}CO gas resulted in a further >20 cm^{-1} down-shift of bands β and δ, indicative of a second ^{13}CO ligand at Fe_d (**iii**). In the dark, species **iii** was converted under ^{12}CO gas to a state differing from unlabeled H_{ox}-CO in band β, suggesting a d_1^{13}CO exchange (**v**). Blue light irradiation of **iii** under ^{13}CO caused an exclusive ~40 cm^{-1} down-shift of band α while β, γ, and δ remained unchanged. Thus, a state with three shifted CO bands with respect to unlabeled H_{ox}-CO was populated, suggesting two distal ^{13}CO ligands and μ^{13}CO (**vi**). Exchange to a ^{12}CO atmosphere resulted in a ~30 cm^{-1} upshift of band δ, small shifts to higher frequencies of β and γ, and no change of band α. This agrees with d_1^{13}CO and μ^{13}CO labeling (**viii**). Red light irradiation of **viii** under ^{12}CO yielded a state showing similar β, γ, and δ frequencies as **xii**, but α remained at its low frequency so that only μ^{13}CO was present (**ix**). ^{13}CO exposure converted **ix** to a state reminiscent of spectrum **ii**, including d_2^{13}CO and μ^{13}CO labeling (**xi**). Finally, blue light irradiation of **xi** under ^{12}CO regained unlabeled H_{ox}-CO (**xii**). These results suggested that μCO and the distal carbonyls were exchangeable in HYDA1, but not the proximal CO ligand.

At increased humidity of the ^{13}CO aerosol and blue light irradiation, HYDA1 with three ^{13}CO ligands (**vi**) produced down-shifts of all four CO bands compared to the unlabeled species. This state was assigned to completely ^{13}CO-labeled H_{ox}-CO (33), including the proximal CO ligand (Fig. 2B, **xii**). Exposure to ^{12}CO caused a ~40 cm^{-1} up-shift of δ with only minor changes for γ and β and no difference for α (**ii**). Further red light irradiation mainly up-

shifted band γ by ~40 cm^{-1} (**iii**). This suggested stepwise replacement of the two ^{13}CO ligands at Fe_d by ^{12}CO in the presence of $p^{13}CO$. Further ^{12}CO exposure under blue light induced the exchange of μCO as indicated by a ~40 cm^{-1} up-shift of band α (**vi**). Rebinding of ^{13}CO to **iii** or **vi** yielded species **v** or **viii**, their δ band positions suggesting a single distal ^{13}CO ligand. Red light irradiation under ^{13}CO of **viii** restored the frequency pattern of **xii** except for the down-shifted band α (**ix**). The latter was exchanged only under blue light (**xii**). ^{12}CO exposure of **viii** finally regained species **ii**. Selective ^{13}CO editing of *p*CO was facilitated only in sufficiently hydrated HYDA1 protein films.

Complementary ^{13}CO editing experiments were performed for CPI and DDH (SI Appendix, Fig. S8). ^{13}CO exchange of the two distal carbonyls was achieved already under red light in these enzymes, possibly related to increased light absorption in the presence of the accessory iron-sulfur clusters, whereas HYDA1 allowed sequential editing with red and blue light. Four of the eight possible H_{ox}-CO isotopic species excluding $p^{13}CO$ were populated in the bacterial enzymes. The CO frequencies, however, were similar in the three enzymes.

H_{ox}-CO isotopic species assignment from DFT. The IR experiments showed 16 distinct H_{ox}-CO isotopic species with all possible labeling patterns. We calculated IR spectra for 96 H_{ox}-CO models, including 16 possible ^{13}CO-labeling patterns with six CO/CN^- rotamers each (SI Appendix, Fig. S12, Table S2). Similarly large rmsd values (~30 cm^{-1}) were observed for all isotopic species with an apical *d*CO, which precluded assignment of the experimental IR spectra for the "standard" H_{ox}-CO geometry. Species with an apical dCN^- showed significantly diminished rmsd values for all isotopic labeling patterns. These results facilitated the unambiguous attribution of each IR spectrum to a specific H_{ox}-CO species (Table 1). Both "medium" and "large" models showed diminished preference for the dCN^- rotamer compared to the "small" H-cluster model (Table S2), but still a two-fold smaller rmsd

was observed for the structure with an apical *d*CN^- ligand. Comprehensive analysis of experimental and calculated IR band frequencies and intensities suggested that H_{ox}-CO structures with proximal CO/CN^- inversion were disfavored and further supported an apical *d*CN^- (Table S4). These results indicated the cyclic isotope editing sequence shown in Fig. 5. The exogenous CO ligand (d_2CO) is exchangeable in darkness, red light sensitivity is attributed to the equatorial d_1CO, and blue light induces exchange of μCO and *p*CO, the latter being feasible only in sufficiently hydrated HYDA1 protein films.

Site-selective ^{13}CO editing and rotamers of H_{ox}. Quantitative population of four H_{ox} isotopic species with zero to two ^{13}CO ligands excluding *p*CO was achieved by N_2 gas exposure of HYDA1 protein films at low humidity (Fig. 2A). H_{ox}-CO species **xii** and **ii** were converted into unlabeled H_{ox} (**i**). In comparison to **i**, H_{ox}-CO species **iii** and **v** were converted into a state showing a ~30 cm^{-1} down-shift of band β and a smaller shift of γ, implying a single ^{13}CO ligand at Fe_d (d^{13}CO) (**iv**). Species **vi** and **viii** yielded a H_{ox} state similar to **iv**, but showing an additional ~40 cm^{-1} down-shift of α due μ^{13}CO labeling (**vii**). Finally, species **ix** and **xi** were converted into a state with an exclusive ~40 cm^{-1} down-shift of α compared to unlabeled H_{ox}, indicative of μ^{13}CO (**x**). Starting with completely ^{13}CO-labeled and hydrated HYDA1 in the H_{ox}-CO state, four H_{ox} species with one to three ^{13}CO ligands including *p*CO were populated by N_2 exposure (Fig. 2B). H_{ox}-CO species **ii** and **xii** were converted to H_{ox} species **i** with bands α, γ, and β shifted ~40 cm^{-1} to lower frequencies (complete ^{13}CO exchange). H_{ox}-CO species with ^{13}CO at Fe_p (p^{13}CO) and ^{12}CO at Fe_d (**iv** and **vii**) were converted to H_{ox} species **iv** and **vii** showing a γ band intensity (1955 cm^{-1}) exceeding the one of band β (1905 cm^{-1}), which was reversed for H_{ox} species with unlabeled *p*CO. These are the only H_{ox} isomers with pronounced vibrational coupling of *d*CO and *p*CO (SI Appendix, Fig.

S9). H_{ox}-CO species **ix** and **xi** finally were converted to H_{ox} species **x**, which resembled species **i** except for presence of μ^{12}CO.

IR band patterns for the 56 possible H_{ox} structures (7 CO/CN^- rotamers with 8 ^{13}CO-labeling patterns each) were calculated (Tables S1). Comparison of experimental and calculated CO frequencies revealed by far lowest rmsd values only for isotopic patterns in agreement with the above experimental assignments (Table 1). In-depth analysis of IR band frequencies and intensities of H_{ox} (SI Appendix, Table S1 and Fig. S11) and mutual comparison to the results for H_{ox}-CO (Table S4) excluded *d*CO in more apical position. On the other hand, the calculated IR data of a structure with *d*CN^- rotated towards a more apical position were as well in agreement with the experimental data as the "standard" ligand configuration, for all isotopic species of H_{ox} (Table 1). Both these structures accounted for vibrational coupling of *p*CO and *d*CO in the presence of a proximal ^{13}CO (SI Appendix, Fig. S9), which explained the inverted intensity ratio of the β and γ bands in H_{ox} species **iv** and **vii**.

Discussion

Our protocol for controlled gas exposure, irradiation, and hydration of [FeFe]-hydrogenase protein films facilitates quantitative population of eight H_{ox} and 16 H_{ox}-CO species selectively labeled with zero to four ^{13}CO ligands, most of which are reported here for the first time. Fourier-transform IR spectroscopy in ATR configuration facilitates rapid gas exchange for controlled and quantitative state population in [FeFe]-hydrogenase protein films. These experiments have provided an unprecedentedly large IR data set for comparison with quantum chemical calculations. The CO vibrational modes underlying the IR spectra were assigned unambiguously. In H_{ox}, experimentally observed CO stretching frequencies are well separated and differ by at least 24 cm^{-1} (pCO/ dCO). This facilitates direct band assignment via ^{13}CO isotope editing. In contrast to H_{ox}, the three terminal carbonyls in H_{ox}-CO show

pronounced vibrational coupling that results from changes in ligand geometry and $[2Fe]_H$ spin distribution (24-28, 31, 36). Disentangling of spectral shifts as induced by stepwise isotope editing of H_{ox}-CO was achieved via DFT analysis. Our results imply a consistent reaction cycle for isotopic editing of the H-cluster (Fig. 5).

H_{ox}-CO in "standard" configuration (27, 46) is not in good agreement with the experimental carbonyl vibrations. Models comprising an apical CN^- ligand at Fe_d yielded a vibrationally uncoupled proximal carbonyl ligand, which is a characteristic feature of the H-cluster (24, 26). Only these models reproduced the altered vibrational origin of the *p*CO IR frequency and inverted band intensities for species including d_1^{13}CO and d_2^{13}CO. Improved correlation of experimental and calculated IR data for H_{ox}-CO with apical *d*CN^- has been discussed before, but evaluated versus insufficiently small experimental IR data sets (39, 47, 48). We prove the effect for 16 H_{ox}-CO species, three phylogenetically distinct [FeFe]-hydrogenases, and varying computational approaches. However, our analysis clearly supports the ligand arrangement at the proximal iron ion in the crystallographic data (21-23).

Available H-cluster structures were modelled with *trans* equatorial carbonyls and square-pyramidal (H_{ox}) or octahedral geometries (H_{ox}-CO) at the distal iron ion (21-23, 27, 46, 49). At a resolution of ~1.5 Å or less, however, CO/CN^- discrimination remains speculative. These ligands originally were assigned using potential hydrogen bonding of CN^- ligands to protein residues (21, 40, 49-51) (SI Appendix, Fig. S10) and before the identity of the adt ligand was unraveled (19). A computational study on the DDH crystal structure preferred the "standard" H_{ox}-CO geometry by ~6 kJ/mol due to interaction of *d*CN^- with a backbone amine and the conserved Lys237 (39, 48). An interaction between Lys237 and *d*CN^- has also been inferred from EPR but was not supported later (20, 52). Our analysis for all model structures suggests slight distortion of octahedral Fe_d symmetry in the "standard" model whereas for an apical CN^- weak H-bonding to the adt nitrogen base occurs (Fig. 4).

This geometry was earlier calculated to be stabilized by ~8 kJ/mol (48). It has been suggested that H_2 may form a similar H-bond to adt during the catalytic reaction (37, 49, 51, 53). Substrate (H_2) or inhibitor (CO) binding at the active site thus may be governed by intramolecular rather than protein-cofactor interactions. The detailed influence of the protein environment on the fine structure of the H-cluster is difficult to quantify both from experimental and theoretical viewpoints. Our general isotope editing scheme (Fig. 5), however, remains valid irrespective of the precise angular arrangement of the distal ligands.

The H_{ox} "standard" configuration (21-23, 49) as well as a rotamer with more apical CN^- and equatorial vacancy at Fe_d showed similar and superior agreement between experimental and calculated IR data. Accordingly, such structures appear equally probable. Our analysis further favors *trans* orientation of equatorial carbonyls and a proximal CO/CN^- arrangement as in crystallographic assignments (21-23, 49). The HYDA1 and CPI proteins used in this study were activated *in vitro* with a synthetic diiron site analogue (39, 40). We observed no significant differences between our HYDA1 and CPI preparations and the natively maturated DDH so that rotamer formation during *in vitro* maturation can be excluded (12, 17, 20, 32, 54). Our observation that only sufficient hydration of HYDA1 protein films facilitates isotope editing at the proximal iron ion rather indicates that structural flexibility of gas channels (55) is involved in ligand exchange. Under cryogenic conditions (i.e. for diffraction data collection), the "standard" H_{ox} structure thus dominates. Biologically relevant conditions (i.e. dissolved protein at room temperature as used here), could promote equilibrium between the two ligand geometries at Fe_d or even dominance of the rotamer with more apical dCN^-. Such equilibria exist for diiron compounds in solution (56-58). This view is further reinforced by molecular dynamics simulations on DDH showing that distal ligand rotation is related to motions by up to 2 Å of a nearby phenylalanine side chain (36). Only in

the rotated H_{ox} structure, CO can bind in equatorial position at Fe_d (Fig. 4). This also impacts on possible motifs of substrate (H_2) interactions with the active site.

H_{ox} is the entry point to the hydrogen conversion cycle of [FeFe]-hydrogenases (1). At least two increasingly reduced H-cluster species were derived from H_{ox}; their molecular structures and involvement in catalysis yet remain to be defined (11-15, 36, 59). The fate of the Fe-Fe bridging carbonyl is of particular mechanistic interest. Binding of hydrogen species in apical position at Fe_d of the H-cluster is believed to be essential for catalysis (1). However, configurations with (semi-) bridging or equatorial H-species were considered as well (12, 14, 36) and may result from structural flexibility of the H-cluster (36). Such structural dynamics may facilitate apical or equatorial ligand binding at the distal iron ion. This may also be relevant for O_2 inactivation of the enzymes via reactive oxygen species formation (24, 29, 30, 60, 61). Our protocol for selective preparation of H_{ox} with eight distinct isotopic labeling patterns introduces spectroscopic probes at individual positions at the cofactor. This opens the road for investigations on novel isotopically labeled intermediates in the catalytic cycle to probe structural dynamics during the H_2-conversion chemistry of [FeFe]-hydrogenases.

Materials and Methods

***HYDA1 protein* preparation.** [FeFe]-hydrogenase HYDA1 and CPI apo-proteins were over-expressed in *Escherichia coli*, purified, and quantitatively reconstituted in vitro with a synthetic diiron complex ($Fe_2(\mu\text{-adt})(CO)_4(CN)_2$, adt = $(SCH_2)_2NH$) (23, 41). All protein preparation and handling procedures were carried out under strictly anoxic conditions and dim light. DDH was purified from *D. desulfuricans* with a complete H-cluster (43).

Infrared spectroscopy. ATR-FTIR spectroscopy (62) was performed with a Tensor27 spectrometer (Bruker) placed in an anaerobic glovebox and equipped with a mid–IR globar, a liquid-nitrogen cooled MCT detector, and a silicon prism with two active reflections, which

was capped by a sealed PCTFE head-space gas compartment. Infrared spectra were recorded with 1 cm^{-1} spectral resolution using varying numbers of interferometer scans on thin protein films, corrected for background contributions, and evaluated using a least-squares fit algorithm. Hydrogenase films were exposed to ^{13}CO, ^{12}CO, or N_2 gas by fast exchange of the head-space atmosphere using a multi-channel mass flow controller (Sierra Instruments) at room temperature. All gases were sent *pro rata* through a water-filled wash bottle to create an aerosol that prevents dehydration of protein films. This allowed controlling the water/ protein ratio in the film ("hydration") and influenced the velocity of any gas-processing reaction. "Humidity" refers to the water/ gas ratio in the aerosol. A Schott white light source with band pass filters (center wavelengths 640 nm or 460 nm) was used for irradiation of protein samples. Details on real-time ATR-FTIR experiments and data evaluation are given in the Supporting Information (SI Appendix, Figs. S1-S4).

Quantum chemical calculations. DFT calculations on H-cluster model structures with $^{12}CO/^{13}CO$ ligands were carried out using Gaussian09 (63) on the Soroban computer cluster of the Freie Universität Berlin. Starting structures of increasing complexity (SI Appendix, Fig. S5) were constructed using the crystal structure of CO-inhibited CPI [FeFe]-hydrogenase (27) as a template and geometry-optimized using the BP86/TZVP or TPSSh/TZVP functional/basis-set combinations (64-66) and IR spectra were calculated thereafter (67). Details of the computational methods are given in the Supporting Information.

Acknowledgements

The authors thank T. Happe and M. Winkler for generously providing protein samples (HYDA1, CPI) and extensive discussion. We are indebted to J. Fontecilla-Camps for providing a sample of DDH protein. M.S. and S.T.S. thank the International Max Plank Research School (IMPRS) on Multiscale Biosystems and the Focus Area NanoScale (Freie

Universität Berlin) for financial support. M.H. gratefully acknowledges funding by the Deutsche Forschungsgemeinschaft (DFG) (grant Ha3265/6-1) and the Bundesministerium für Bildung und Forschung (grant 05K14KE1). J.D. acknowledges support by the China Scholarship Council (CSC). U.-P.A. and F.W. are grateful for financial support by the Fonds of the Chemical Industry (Liebig grant to U.-P.A.) and the Deutsche Forschungsgemeinschaft (Emmy Noether grant to U.-P.A., AP242/2-1).

References

1. Lubitz W, Ogata H, Rudiger O, & Reijerse E (2014) Hydrogenases. *Chem Rev* 114(8):4081-4148.

2. Peters JW & Broderick JB (2012) Emerging paradigms for complex iron-sulfur cofactor assembly and insertion. *Annu Rev Biochem* 81:429-450.

3. Stripp ST & Happe T (2009) How algae produce hydrogen--news from the photosynthetic hydrogenase. *Dalton Trans* (45):9960-9969.

4. Armstrong FA & Fontecilla-Camps JC (2008) Biochemistry. A natural choice for activating hydrogen. *Science* 321(5888):498-499.

5. Madden C, *et al.* (2012) Catalytic turnover of [FeFe]-hydrogenase based on single-molecule imaging. *J Am Chem Soc* 134(3):1577-1582.

6. Simmons TR, Berggren G, Bacchia M, Fontecave M, & Artero V (2014) Mimicking hydrogenases: from biomimetics to artificial enzymes. *Coord Chem Rev* 270-271:127-150.

7. Rauchfuss TB (2007) Chemistry. A promising mimic of hydrogenase activity. *Science* 316(5824):553-554.

8. Artero V, *et al.* (2015) From enzyme maturation to synthetic chemistry: the case of hydrogenases. *Acc Chem Res* 48(8):2380-2387.

9. Dubini A & Ghirardi ML (2015) Engineering photosynthetic organisms for the production of biohydrogen. *Photosynth Res* 123(3):241-253.

10. Lewis NS & Nocera DG (2006) Powering the planet: chemical challenges in solar energy utilization. *Proc Natl Acad Sci U S A* 103(43):15729-15735.

11. Adamska-Venkatesh A, *et al.* (2014) New redox states observed in [FeFe] hydrogenases reveal redox coupling within the H-cluster. *J Am Chem Soc* 136(32):11339-11346.

12. Adamska A, *et al.* (2012) Identification and characterization of the "super-reduced" state of the H-cluster in [FeFe] hydrogenase: a new building block for the catalytic cycle? *Angew Chem Int Ed Engl* 51(46):11458-11462.

13. Lambertz C, *et al.* (2014) Electronic and molecular structures of the [2Fe] and [4Fe4S] units of the active-site H-cluster in [FeFe]-hydrogenase determined by spin- and site-selective XAE and DFT. *Chem Sci* 5:1187-1203.

14. Chernev P, *et al.* (2014) Hydride binding to the active site of [FeFe]-hydrogenase. *Inorg Chem* 53(22):12164-12177.

15. Mulder DW, *et al.* (2013) EPR and FTIR analysis of the mechanism of H2 activation by [FeFe]-hydrogenase HydA1 from *Chlamydomonas reinhardtii*. *J Am Chem Soc* 135(18):6921-6929.

16. De Lacey AL, Fernandez VM, Rousset M, & Cammack R (2007) Activation and inactivation of hydrogenase function and the catalytic cycle: spectroelectrochemical studies. *Chem Rev* 107(10):4304-4330.

17. Gilbert-Wilson R, *et al.* (2015) Spectroscopic investigations of [FeFe] hydrogenase maturated with [(57)Fe2(adt)(CN)2(CO)4](2.). *J Am Chem Soc* 137(28):8998-9005.

18. Kuchenreuther JM, *et al.* (2014) The HydG enzyme generates an Fe(CO)2(CN) synthon in assembly of the FeFe hydrogenase H-cluster. *Science* 343(6169):424-427.

19. Silakov A, Wenk B, Reijerse E, & Lubitz W (2009) (14)N HYSCORE investigation of the H-cluster of [FeFe] hydrogenase: evidence for a nitrogen in the dithiol bridge. *Phys Chem Chem Phys* 11(31):6592-6599.

20. Adamska-Venkatesh A, *et al.* (2015) Spectroscopic characterization of the bridging amine in the active site of [FeFe] hydrogenase using isotopologues of the H-cluster. *J Am Chem Soc* 137(40):12744-12747.

21. Peters JW, Lanzilotta WN, Lemon BJ, & Seefeldt LC (1998) X-ray crystal structure of the Fe-only hydrogenase (CpI) from *Clostridium pasteurianum* to 1.8 angstrom resolution. *Science* 282(5395):1853-1858.

22. Nicolet Y, Piras C, Legrand P, Hatchikian CE, & Fontecilla-Camps JC (1999) *Desulfovibrio desulfuricans* iron hydrogenase: the structure shows unusual coordination to an active site Fe binuclear center. *Structure* 7(1):13-23.

23. Esselborn J, *et al.* (2016) A structural view of synthetic cofactor integration into [FeFe]-hydrogenases. *Chem Sci* DOI: 10.1039/C5SC03397G.

24. Roseboom W, De Lacey AL, Fernandez VM, Hatchikian EC, & Albracht SP (2006) The active site of the [FeFe]-hydrogenase from *Desulfovibrio desulfuricans*. II. Redox properties, light sensitivity and CO-ligand exchange as observed by infrared spectroscopy. *J Biol Inorg Chem* 11(1):102-118.

25. Chen Z, *et al.* (2002) Infrared studies of the CO-inhibited form of the Fe-only hydrogenase from *Clostridium pasteurianum* I: examination of its light sensitivity at cryogenic temperatures. *Biochemistry* 41(6):2036-2043.

26. De Lacey AL, Stadler C, Cavazza C, Hatchikian EC, & Fernandez VM (2000) FTIR characterization of the active site of the Fe-hydrogenase from *Desulfovibrio desulfuricans*. *J Am Chem Soc* 122:11232-11233.

27. Lemon BJ & Peters JW (1999) Binding of exogenously added carbon monoxide at the active site of the iron-only hydrogenase (CpI) from *Clostridium pasteurianum*. *Biochemistry* 38(40):12969-12973.

28. Myers WK, *et al.* (2014) The Cyanide Ligands of [FeFe] Hydrogenase: Pulse EPR Studies of C-13 and N-15-Labeled H-Cluster. *J Am Chem Soc* 136(35):12237-12240.

29. Stripp ST, *et al.* (2009) How oxygen attacks [FeFe] hydrogenases from photosynthetic organisms. *Proc Natl Acad Sci U S A* 106(41):17331-17336.

30. Silakov A, Wenk B, Reijerse E, Albracht SP, & Lubitz W (2009) Spin distribution of the H-cluster in the H(ox)-CO state of the [FeFe] hydrogenase from Desulfovibrio desulfuricans: HYSCORE and ENDOR study of (14)N and (13)C nuclear interactions. *J Biol Inorg Chem* 14(2):301-313.

31. Pierik AJ, Hulstein M, Hagen WR, & Albracht SP (1998) A low-spin iron with CN and CO as intrinsic ligands forms the core of the active site in [Fe]-hydrogenases. *Eur J Biochem* 258(2):572-578.

32. Silakov A, Kamp C, Reijerse E, Happe T, & Lubitz W (2009) Spectroelectrochemical characterization of the active site of the [FeFe] hydrogenase HydA1 from *Chlamydomonas reinhardtii*. *Biochemistry* 48(33):7780-7786.

33. Kuchenreuther JM, George SJ, Grady-Smith CS, Cramer SP, & Swartz JR (2011) Cell-free H-cluster synthesis and [FeFe] hydrogenase activation: All five CO and CN ligands derive from tyrosine. *PLoS One* 6(5):e20346.

34. Goldet G, *et al.* (2009) Electrochemical kinetic investigations of the reactions of [FeFe]-hydrogenases with carbon monoxide and oxygen: comparing the importance of gas tunnels and active-site electronic/redox effects. *J Am Chem Soc* 131(41):14979-14989.

35. Siebel JF, *et al.* (2015) Hybrid [FeFe]-hydrogenases with modified active sites show remarkable residual enzymatic activity. *Biochemistry* 54(7):1474-1483.

36. Fourmond V, *et al.* (2014) The oxidative inactivation of FeFe hydrogenase reveals the flexibility of the H-cluster. *Nat Chem* 6(4):336-342.

37. Mulder DW, *et al.* (2014) Investigations on the role of proton-coupled electron transfer in hydrogen activation by [FeFe]-hydrogenase. *J Am Chem Soc* 136(43):15394-15402.

38. Tye JW, Darensbourg MY, & Hall MB (2008) Refining the active site structure of iron-iron hydrogenase using computational infrared spectroscopy. *Inorg Chem* 47(7):2380-2388.

39. Yu L, *et al.* (2011) Targeting intermediates of [FeFe]-hydrogenase by CO and CN vibrational signatures. *Inorg Chem* 50(9):3888-3900.

40. Winkler M, Esselborn J, & Happe T (2013) Molecular basis of [FeFe]-hydrogenase function: An insight into the complex interplay between protein and catalytic cofactor. *Biochim Biophys Acta* 1827(8-9):974-985.

41. Esselborn J, *et al.* (2013) Spontaneous activation of [FeFe]-hydrogenases by an inorganic [2Fe] active site mimic. *Nat Chem Biol* 10(9):607-609.

42. Berggren G, *et al.* (2013) Biomimetic assembly and activation of [FeFe]-hydrogenases. *Nature* 499(7456):66-69.

43. Hatchikian EC, Forget N, Fernandez VM, Williams R, & Cammack R (1992) Further characterization of the [Fe]-hydrogenase from *Desulfovibrio desulfuricans* ATCC 7757. *Eur J Biochem* 209(1):357-365.

44. Gonzales MA & Mascharak PK (2014) Photoactive metal carbonyl complexes as potential agents for targeted CO delivery. *J Inorg Biochem* 133:127-135.

45. van der Spek TM, *et al.* (1996) Similarities in the architecture of the active sites of Ni-hydrogenases and Fe-hydrogenases detected by means of infrared spectroscopy. *Eur J Biochem* 237(3):629-634.

46. Pandey AS, Harris TV, Giles LJ, Peters JW, & Szilagyi RK (2008) Dithiomethylether as a ligand in the hydrogenase h-cluster. *J Am Chem Soc* 130(13):4533-4540.

47. Zilberman S, Stiefel EI, Cohen MH, & Car R (2006) Resolving the CO/CN ligand arrangement in CO-inactivated [FeFe] hydrogenase by first principles density functional theory calculations. *Inorg Chem* 45(15):5715-5717.

48. Greco C, *et al.* (2007) Structural insights into the active-ready form of [FeFe]-hydrogenase and mechanistic details of its inhibition by carbon monoxide. *Inorg Chem* 46(18):7256-7258.

49. Nicolet Y, *et al.* (2001) Crystallographic and FTIR spectroscopic evidence of changes in Fe coordination upon reduction of the active site of the Fe-only hydrogenase from *Desulfovibrio desulfuricans*. *J Am Chem Soc* 123(8):1596-1601.

50. Knorzer P, *et al.* (2012) Importance of the protein framework for catalytic activity of [FeFe]-hydrogenases. *J Biol Chem* 287(2):1489-1499.

51. Bruschi M, *et al.* (2009) Influence of the [2Fe]H subcluster environment on the properties of key intermediates in the catalytic cycle of [FeFe] hydrogenases: hints for the rational design of synthetic catalysts. *Angew Chem Int Ed Engl* 48(19):3503-3506.

52. Silakov A, Reijerse EJ, Albracht SP, Hatchikian EC, & Lubitz W (2007) The electronic structure of the H-cluster in the [FeFe]-hydrogenase from *Desulfovibrio desulfuricans*: a Q-band 57Fe-ENDOR and HYSCORE study. *J Am Chem Soc* 129(37):11447-11458.

53. Rauchfuss TB (2015) Diiron azadithiolates as models for the [FeFe]-hydrogenase active site and paradigm for the role of the second coordination sphere. *Acc Chem Res* 48(7):2107-2116.

54. Adamska-Venkatesh A, *et al.* (2015) Artificially maturated [FeFe] hydrogenase from Chlamydomonas reinhardtii: a HYSCORE and ENDOR study of a non-natural H-cluster. *Phys Chem Chem Phys* 17(7):5421-5430.

55. Cohen J, Kim K, King P, Seibert M, & Schulten K (2005) Finding gas diffusion pathways in proteins: application to O2 and H2 transport in CpI [FeFe]-hydrogenase and the role of packing defects. *Structure* 13(9):1321-1329.

56. Leidel N, *et al.* (2012) Electronic structure of an [FeFe] hydrogenase model complex in solution revealed by X-ray absorption spectroscopy using narrow-band emission detection. *J Am Chem Soc* 134(34):14142-14157.

57. Bethel RD, *et al.* (2015) Regioselectivity in ligand substitution reactions on diiron complexes governed by nucleophilic and electrophilic ligand properties. *Inorg Chem* 54(7):3523-3535.

58. Barton BE, *et al.* (2010) Isomerization of the hydride complexes [HFe2(SR)2(PR3)(x)(CO)(6-x)]+ (x = 2, 3, 4) relevant to the active site models for the [FeFe]-hydrogenases. *Dalton Trans* 39(12):3011-3019.

59. Hajj V, *et al.* (2014) FeFe hydrogenase reductive inactivation and implication for catalysis. *Energy Environ Sci* 7:715-719.

60. Lambertz C, *et al.* (2011) O2 reactions at the six-iron active site (H-cluster) in [FeFe]-hydrogenase. *J Biol Chem* 286(47):40614-40623.

61. Swanson KD, *et al.* (2015) [FeFe]-hydrogenase oxygen inactivation is initiated at the H cluster 2Fe subcluster. *J Am Chem Soc* 137(5):1809-1816.

62. Nyquist RM, Ataka K, & Heberle J (2004) The Molecular Mechanism of Membrane Proteins Probed by Evanescent Infrared Waves. *ChemBioChem* 3(431): 431-436.

63. Frisch MJT, *et al.* (2009) Gaussian 09, Revision D.01. *Gaussian, Inc., Wallingford CT.*

64. Tao JM, Perdew JP, Staroverov VN, & Scuseria GE (2003) Climbing the density functional ladder: Nonempirical meta-generalized gradient approximation designed for molecules and solids. *Phys Rev Lett* 91(14):146401.

65. Schäfer A, Huber C, & Ahlrichs R (1994) Fully optimized contracted Gaussian basis sets of triple zeta valence quality for atoms Li to Kr. *J Chem Phys* 100(8):5829-5835.

66. Becke AD (1988) Density-functional exchange-energy approximation with correct asymptotic behavior. *Phys Rev A* 38(6):3098-3100.

67. Ponec R (2015) Structure and bonding in binuclear metal carbonyls. Classical paradigms vs. insights from modern theoretical calculations. *Comput Theor Chem* 1053:195-213.

Figures

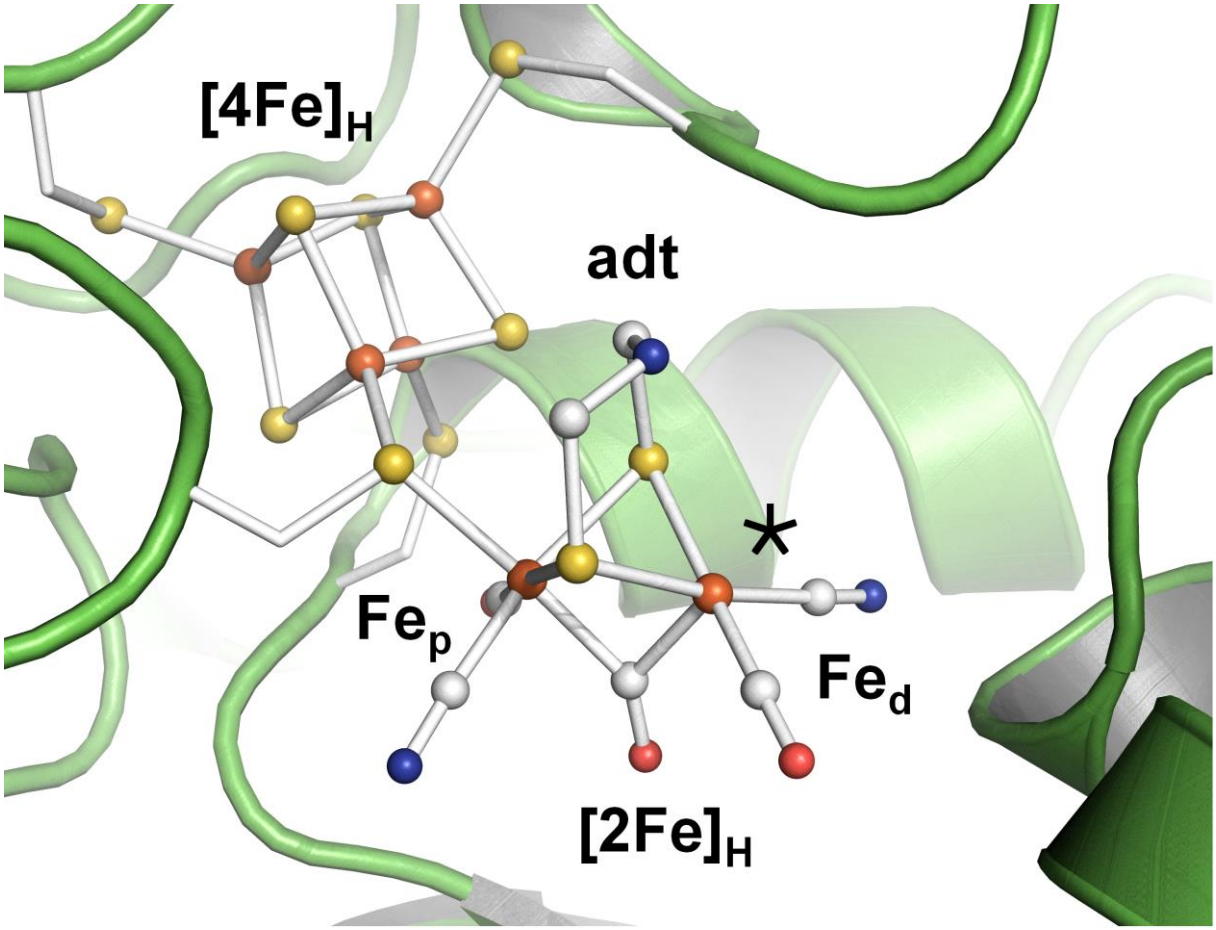

Figure 1: Crystal structure of [FeFe]-hydrogenase from *Clostridium pasteurianum* (23). The H-cluster (ball-and-stick) with its cubane ($[4Fe4S]_H$) and diiron sub-complexes ($[2Fe]_H$ with an amine-dithiolate = adt bridge) is protein-bound by four cysteine residues. An apical vacant site (*) at Fe_d was modeled in structures of oxidized enzymes (21-23, 46). The shown CO/CN^- ligand orientation herein is annotated "standard".

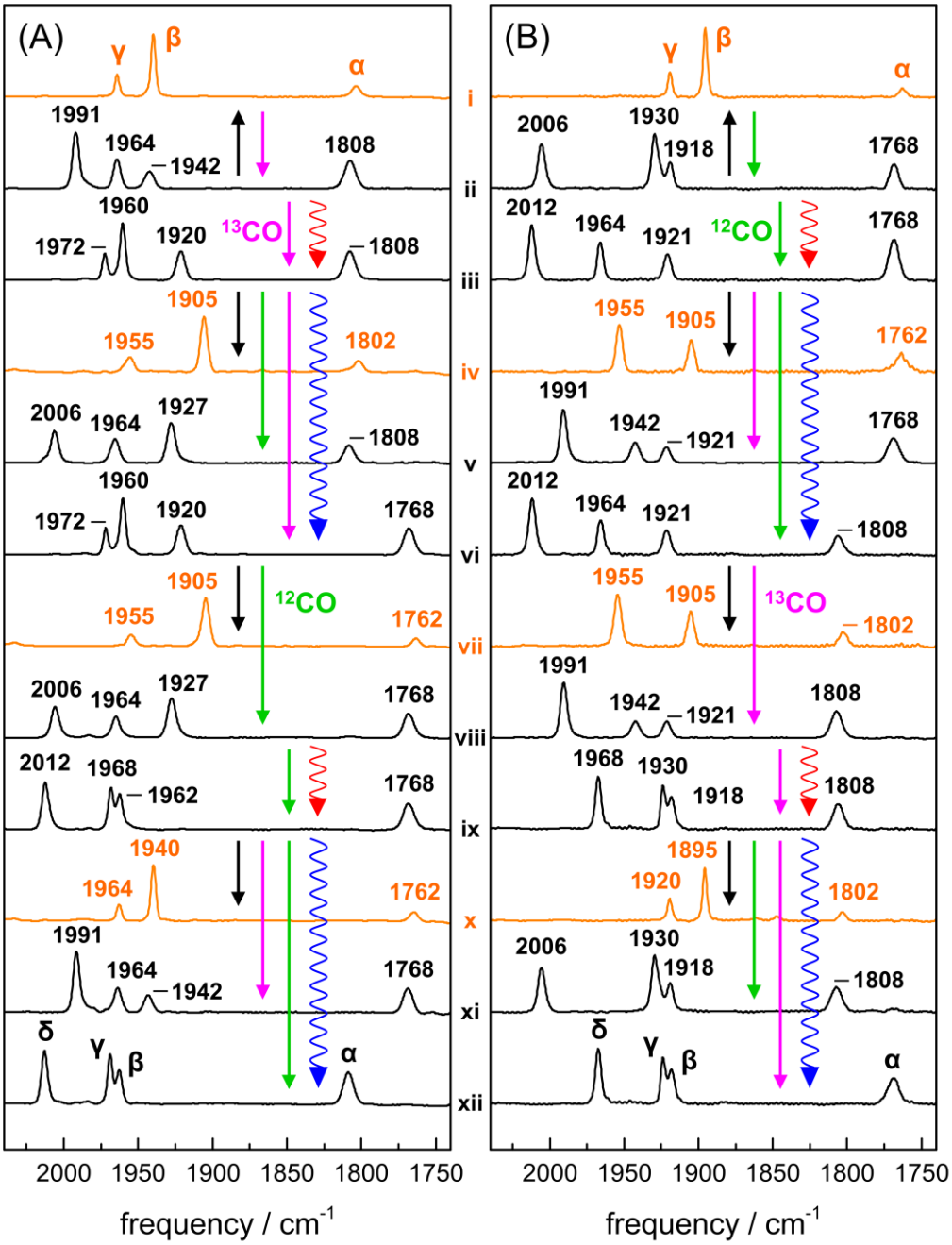

Figure 2: ATR-FTIR spectra of HYDA1 [FeFe]-hydrogenase films. (A) Isotopic species with a p^{12}CO ligand. (B) Isotopic species with a p^{13}CO ligand. IR bands due to stretching vibrations of CO ligands at the H-cluster were normalized to unity area sums. Spectra are attributed to H_{ox} (orange) or H_{ox}-CO (black); CO bands are denoted α, β, γ, and δ. For real-time ATR-FTIR experiments see SI Appendix, Fig. S3. Straight arrows denote gas exposures (^{12}CO, green; ^{13}CO, magenta; N_2, black), wiggled arrows denote red or blue light irradiation. Numerals **i-xii** annotates identified spectral species (Table 1).

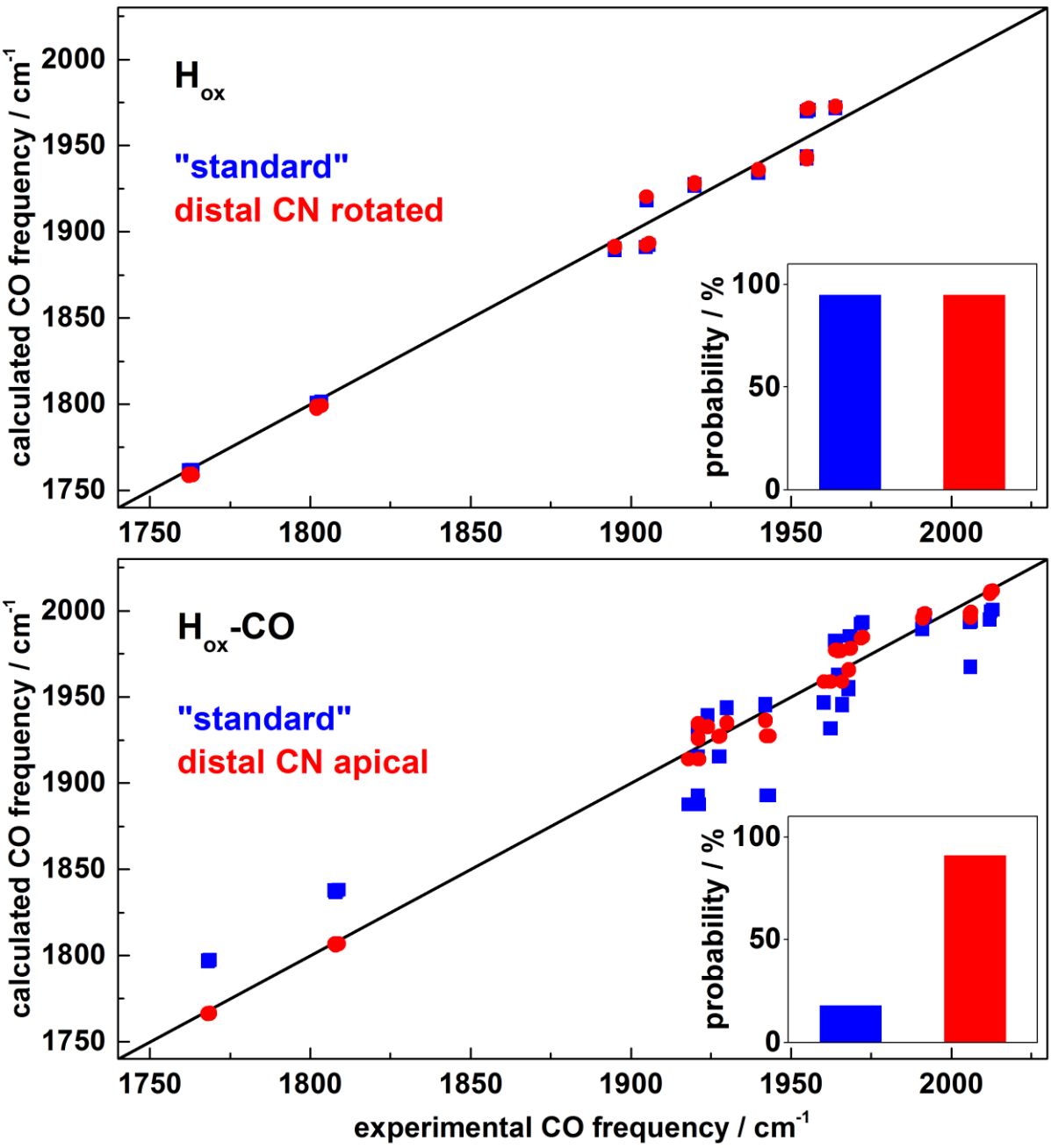

Figure 3: Correlation of experimental and calculated CO band frequencies. (A) H_{ox}: "standard" model (blue) and model with proximal CN^- rotated towards apical position (red). (B) H_{ox}-CO: "standard" model (blue) and model with distal CN^- in apical position (red). Diagonals show ideal correlation. Calculated CO frequencies were offset-corrected (31±1 cm^{-1}, H_{ox}; 38±2 cm^{-1}, H_{ox}-CO) for alignment with experimental data (Tables S1, S2). Insets: approximate rotamer probabilities from IR data analysis (Table S4).

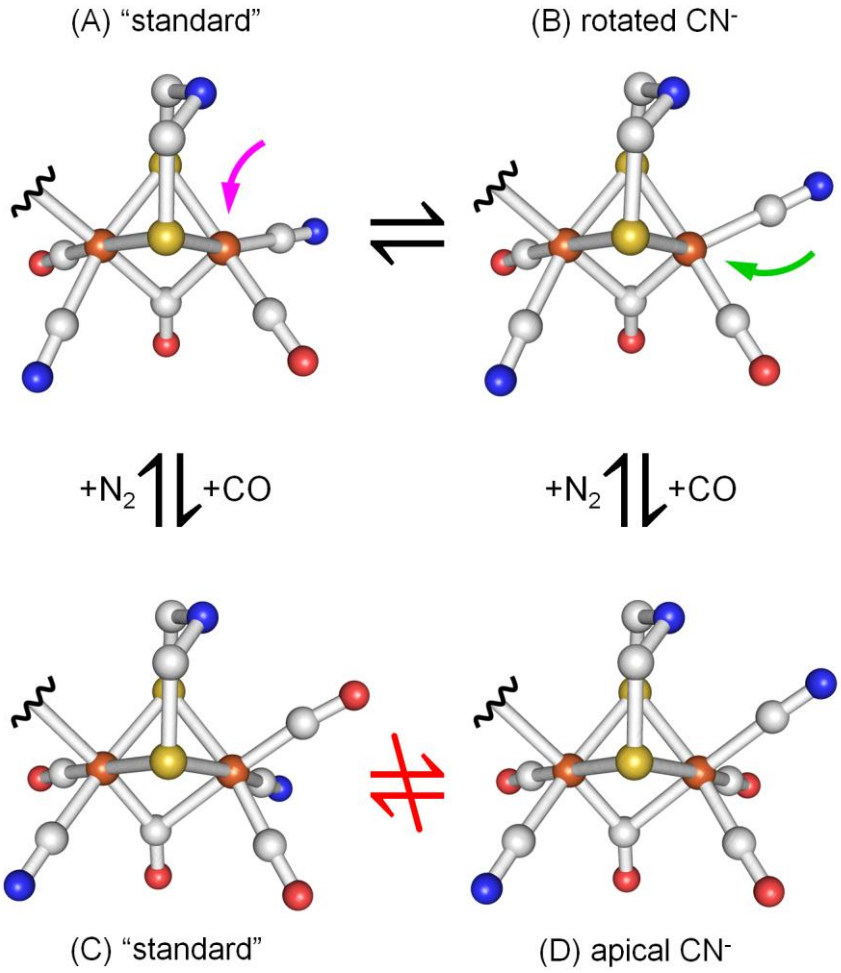

Figure 4: H-cluster rotamer structures of H_{ox} and H_{ox}-CO. A transition from H_{ox} structure (A) to H_{ox}-CO structure (C) is suggested in the "standard" model where exogenous CO binds at Fe_d in apical position (magenta arrow). Equilibrium between H_{ox} rotamers (A) and (B) facilitates CO binding at Fe_d in equatorial position (green arrow) and thereby transition to the H_{ox}-CO rotamer with apical CN^- at Fe_d (D). Octahedral coordination of Fe_d in H_{ox}-CO renders ligand rotation unlikely and prevents a transition between rotamers (C) and (D).

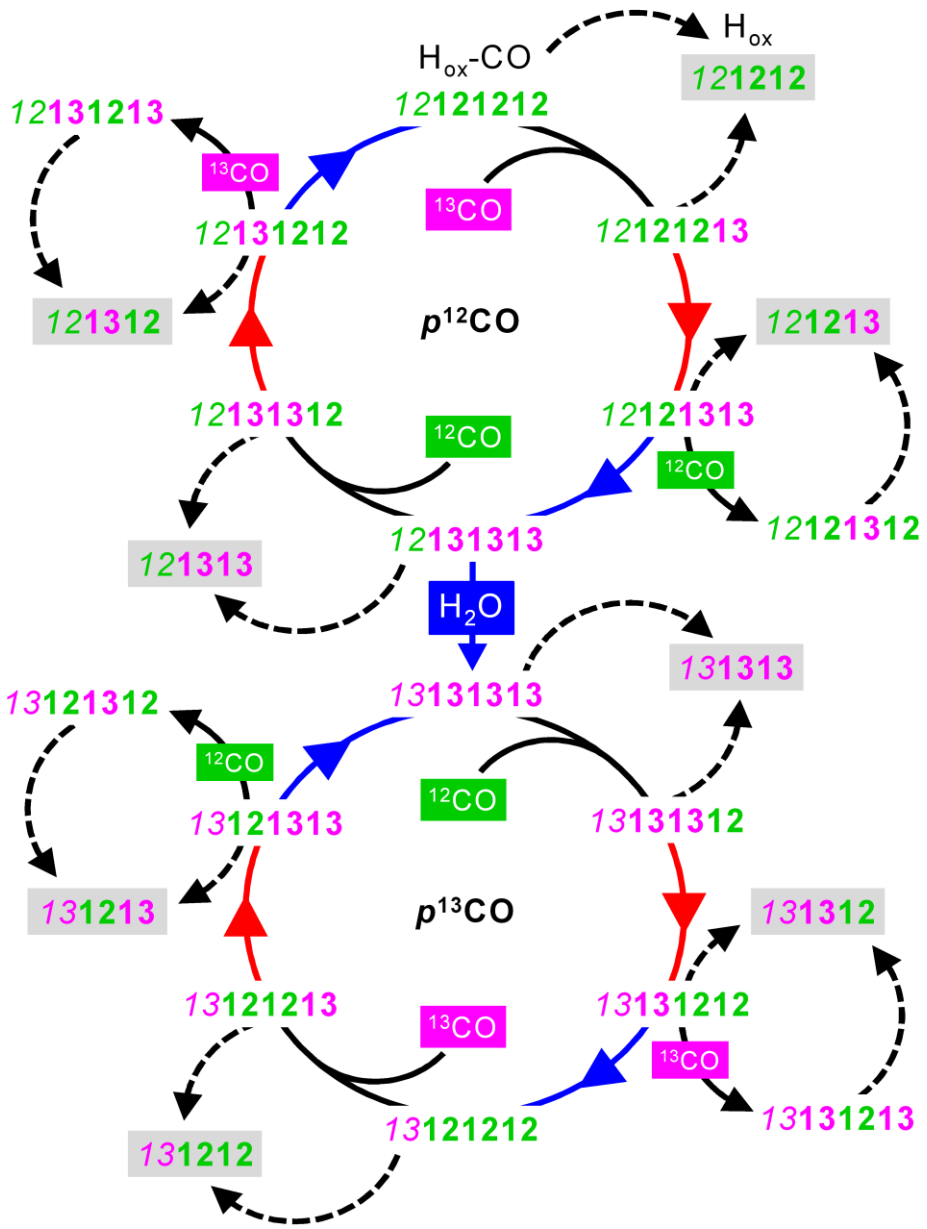

Figure 5: Stepwise isotope editing of the H-cluster. Grey shadings highlight eight differently labeled H_{ox} species providing access to the catalytic cycle of hydrogen turnover. Carbonyl ligand patterns are shown in the order p μ d_1 d_2 (d_2 is present only in H_{ox}-CO). Exposure to ^{13}CO (magenta) or ^{12}CO (green) gas is indicated only for the dark steps (solid black arrows) and persisted during the following "red" or "blue" light irradiation steps (colored arrows) in the experimental cycle; dashed arrows denote N_2 exposure in darkness. The proximal CO ligand is prone to ^{13}CO exchange only in sufficiently hydrated ("H_2O") protein films.